Author Manuscript

MORPHOLOGICAL AND OPTICAL PROFILING OF MELANOCYTES AND SK-MEL-28 MELANOMA CELLS VIA DIGITAL HOLOGRAPHIC MICROSCOPY AND QUANTITATIVE PHASE IMAGING

Ayah A. Farhat, Yazan A. Almahdi, Fatima Z. Alshuhani, Besa Xhabija

College of Arts Sciences and Letters, Department of Natural Science, University of Michigan-Dearborn, Dearborn, MI, U.S.A.

Correspondence to: Dr. Besa Xhabija, 4901 Evergreen Road, Dearborn, MI 48128, USA. Tel: +1 3135935077, e-mail: xhabija@umich.edu

Short Running Title: Morphological and Optical Analysis of Melanocytes and Melanoma Cells

Key Words: Melanocytes, SK-MEL-28 cells, Melanoma, Digital holographic microscopy, Principal Component Analysis (PCA), t-Distributed Stochastic Neighbor Embedding (t-SNE), Cell motility, Morphology, Optical properties, Cell migration

This is the author manuscript accepted for publication and has undergone full peer review but has not been through the copyediting, typesetting, pagination and proofreading process, which may lead to differences between this version and the Version of Record. Please cite this article as doi: 10.1002/adbi.202400346.

This article is protected by copyright. All rights reserved.

Author Manuscript

Abstract

Melanoma, originating from pigment-producing melanocytes, remains a highly aggressive and deadly form of skin cancer. Despite extensive research, the mechanisms underlying melanoma progression and metastasis are not fully elucidated. This study employs quantitative phase imaging using digital holographic microscopy, Principal Component Analysis (PCA), and t-distributed Stochastic Neighbor Embedding (t-SNE), to delineate the morphological, optical, and behavioral differences between normal melanocytes and SK-MEL-28 melanoma cells. Our findings reveal significant distinctions in cell shape, size, and internal organization, with SK-MEL-28 cells exhibiting greater variability in size, more regular polygonal shapes, and higher optical thickness compared to melanocytes. Moreover, phase shift parameters and surface roughness analyses underscore the more uniform and predictable textures of melanoma cells. Violin plots of cell movement patterns highlight the dynamic and varied migration behaviors of SK-MEL-28 cells, contrasting with the more localized movement of melanocytes. Hierarchical clustering of a correlation matrix provides further insights into the complex relationships between morphological and optical parameters. The integration of label-free quantitative phase imaging and robust analytical methods offers a comprehensive characterization of the distinct features of melanoma cells, enhancing our understanding of melanoma's aggressive behavior and aiding in the development of targeted therapeutic strategies. These findings underscore the potential of morphological and optical biomarkers in differentiating between normal and cancerous cells, paving the way for more precise diagnostic and therapeutic approaches in melanoma treatment.

1. Introduction

This article is protected by copyright. All rights reserved.

Author Manuscript

Melanoma is a highly aggressive form of skin cancer originating from melanocytes, the pigment-producing cells in the epidermis [1-5]. Despite extensive research, the biological mechanisms underlying melanoma progression and metastasis remain incompletely understood, necessitating more detailed studies on cellular morphology, behavior, and molecular characteristics [2, 4, 6-9].

Morphological analysis using advanced imaging techniques can provide critical insights into the structural differences between normal melanocytes and SK-MEL-28 melanoma cells [10-13]. These differences are pivotal for understanding the disease and developing targeted therapeutic strategies [14, 15]. Recent advances in holographic microscopy have enabled detailed visualization of cellular structures, revealing significant differences in cell shape, size, and internal organization[16]. These imaging techniques allow for the examination of parameters such as cell area, optical volume, and thickness, offering a comprehensive view of cellular morphology [11, 16].

Principal Component Analysis (PCA) and t-distributed Stochastic Neighbor Embedding (t-SNE) are powerful tools for reducing the dimensionality of complex morphological data, enabling clear visualization and clustering of cell types based on their morphological features[17]. These analytical methods help distinguish between normal and cancerous cells, providing a robust framework for identifying key morphological markers associated with melanoma. However, t-SNE may outperform PCA plots in terms of visualization and classification accuracy, since t-SNE is more effective at maintaining the local structure of high-dimensional data, which is critical for distinguishing between different classes in the dataset[18].

Further, analyzing cell movement patterns and directionality is crucial for understanding the invasive behavior of melanoma cells. Time-lapse holographic microscopy and subsequent movement analysis at the single-cell level reveal dynamic behaviors that differentiate melanoma cells from normal melanocytes[19]. These movement patterns are essential for

This article is protected by copyright. All rights reserved.

Author Manuscript

studying metastasis and the cellular mechanisms that drive cancer spread [20, 21]. The heterogeneity in molecular and structural characteristics of melanoma cells complicates the disease and underscores the importance of detailed investigations[22-24]. Techniques such as hierarchical clustering and correlation matrix analysis facilitate the identification of relationships between various cellular parameters, enhancing our understanding of melanoma's complexity.

This study aims to characterize the morphological, optical, and behavioral differences between normal melanocytes and SK-MEL-28 melanoma cells using advanced imaging and analytical techniques. By leveraging 2D and pseudo 3D microscopy, PCA, t-SNE, and cell movement analysis, we seek to elucidate the distinct features of melanoma cells that contribute to their aggressive behavior and potential for metastasis. The findings from this research provide valuable insights that could inform the development of more effective diagnostic and therapeutic strategies for melanoma.

2. Materials and Methods

2.1. Cell Culture and Digital Holographic Microscopy

The melanoma cell line SK-MEL-28 (ATCC HTB-72) was cultured in RPMI 1640 (ATCC 30-2001) supplemented with 10% Fetal Bovine Serum (ATCC) and 1% Penicillin-Streptomycin (Thermo Fisher) at 37°C with 5% CO_2. Primary epidermal melanocytes (HEMa, ATCC PCS-200-013) were cultured in Dermal Cell Basal Medium (ATCC PCS-200-030) combined with the Adult Melanocyte Growth Kit (ATCC PCS-200-042) at 37°C with 5% CO_2, with the complete growth medium containing 5 µg/mL rh Insulin, 50 µg/mL Ascorbic Acid, 6 mM L-Glutamine, 1.0 µM Epinephrine, 1.5 mM Calcium chloride, 0.2% Peptide Growth Factor (proprietary formulation), and 1% M8 Supplement (proprietary formulation). Both cell lines were seeded in 24-well plates and analyzed over a 58-hour period using a HoloMonitor M4

This article is protected by copyright. All rights reserved.

Author Manuscript

holographic imaging microscope (Phase Holographic Imaging, Lund, Sweden). The HoloMonitor M4 captured images at 15-minute intervals in each well, with each interval consisting of 30 frames. The App Suite Cell Imaging software analyzed these frames, conducting Guided End-Point Assays (including Cell Quality Control), Guided Kinetic Assays (including Kinetic Proliferation Assay and Kinetic Motility Assay), and In-Depth Assays (including Cell Morphology), providing detailed insights into cell behavior and morphology over the observation period.

2.2. 2D, pseudo 3D Cell Holographic Microscopy

Microscopic 2D images of the Melanocytes and SK-MEL-28 cells were captured via the HoloMonitor M4, which automatically snapped photos of the cells at 15-minute intervals over a 58-hour time period. Under the “Experiment Overview” feature of the App Suite Cell Imaging software, the image color palette was modified via the Coloring panel from a monochromatic scale to a blue-yellow coloring, with the blue indicative of the cells and the yellow indicative of the growth medium. The colors applied are relative to the thickness of the cells, with the scale ranging from -0.5 μm to 20.1 μm.

Individual pseudo 3D images of the Melanocytes and SK-MEL-28 cells were analyzed via the App Suite Cell Imaging software of the HoloMonitor M4. In the “In-Depth Analysis: Single Cell Tracking” package of the software, we converted the 2D images to their respective pseudo 3D structures via modifications of the “Viewer Options” panel. In addition, the color palette was modified under the “Coloring” panel to “Sea,” which applied a pseudo coloring to the image in order to improve visual appeal. The colors are indicative of differences in thickness across the well, with the thickness scale ranging from 0 μm to 16 μm. Relative distances across the cell

This article is protected by copyright. All rights reserved.

Author Manuscript

as well as cell peaks were measured interactively via the “Measure” features under “Viewer Options.” Individual Melanocyte and SK-MEL-28 cell length, width, and peaks were measured by left-clicking at one end of the cell and releasing at the other end. The measured distance is displayed via the blue bar above the cell, and the measurements taken are summarized in the line graph titled "Profile Analysis" at the bottom right of the image.

2.3. Principal Component Analysis and t-Distributed Stochastic Neighbor Embedding analysis of Morphological Features

To analyze and visualize the morphological features of Melanocytes and SK-MEL-28 cells, we employed Principal Component Analysis (PCA) and t-Distributed Stochastic Neighbor Embedding (t-SNE). The dataset analyzed contained various morphological parameters, such as area, perimeter, eccentricity, and optical properties.

For PCA, the dataset was separated into two groups based on cell type: Melanocytes and SK-MEL-28. Numerical columns were selected for PCA analysis, excluding any categorical data. The data for each group was standardized using the *StandardScaler* from the *scikit-learn* library to ensure each feature had a mean of 0 and a standard deviation of 1, which is crucial due to PCA's sensitivity to the variances of the original features. PCA was performed separately on the standardized data for each group, with the number of principal components set to 2 to facilitate visualization in a two-dimensional plot. The PCA transformation resulted in two principal components for each sample, capturing the maximum variance in the data. The principal components of Melanocytes and SK-MEL-28 cells were then plotted on a scatter plot using *matplotlib*, with Melanocytes represented in black and SK-MEL-28 cells in red. This PCA plot provided a visual representation of the morphological differences between Melanocytes and SK-MEL-28 cells, highlighting the variance captured by the principal

This article is protected by copyright. All rights reserved.

components. Furthermore, this plot allows for the identification of patterns and potential clustering within the data, facilitating further biological interpretation and analysis.

For t-SNE, the standardized data for both Melanocytes and SK-MEL-28 cells were combined into a single dataset. t-SNE was performed on this combined dataset using the TSNE class from the *scikit-learn* library. The number of components was set to 2 to facilitate visualization in a two-dimensional plot, and the t-SNE algorithm was run with a random state of 42 for reproducibility. The t-SNE results, consisting of two components for each sample, were plotted on a scatter plot using *matplotlib*, with Melanocytes represented in black and SK-MEL-28 cells represented in red. The resulting t-SNE plot provided a visual representation of the morphological differences between Melanocytes and SK-MEL-28 cells, revealing distinct clusters and patterns in the reduced-dimensional space; this representation thereby aids in understanding the underlying structure and similarities within the high-dimensional morphological data.

2.4. Violin Plots Generation

To compare the morphological features of Melanocytes and SK-MEL-28 cells, we implemented a comprehensive data analysis pipeline to create violin plots. The *pandas* library was utilized to perform data manipulation and analysis on the dataset containing all of the morphological features. The 'Group' column, representing the categorical variable distinguishing Melanocytes and SK-MEL-28 cells, was converted to a string data type to facilitate accurate plotting and visualization. Furthermore, columns containing numeric data were converted to the float data type, with appropriate error handling mechanisms in place to address any potential issues that may have arisen during the conversion process. This preprocessing step ensured that the data was in a suitable format for subsequent analysis and visualization.

This article is protected by copyright. All rights reserved.

Author Manuscript

Author Manuscript

The creation of the violin plots was accomplished using the *seaborn* library, a statistical data visualization tool built on top of *matplotlib*. Seaborn provides a high-level interface for creating informative and visually appealing statistical graphics. For each set of morphological features, such as Area, Boxed breadth, and Boxed length, a separate figure was generated, with subplots dedicated to each individual feature. The violinplot function from *seaborn* was employed to visualize the distribution of each feature, with the 'Group' column represented on the x-axis and the corresponding feature values on the y-axis. To enhance the visual distinction between Melanocytes and SK-MEL-28 cells, the palette parameter was set to assign specific colors to each cell type: black for Melanocytes and red for SK-MEL-28 cells. This color coding facilitated easy identification and comparison of the two cell populations.

To provide clear and informative labels for the plots, appropriate titles were added to each subplot, indicating the specific morphological feature being visualized. The x-axis was labeled as "Cell Type" to denote the categorical nature of the 'Group' column, while the y-axis was labeled with the corresponding feature name, ensuring clarity and interpretability of the plots. To optimize the layout and spacing between subplots, the tight_layout function from *matplotlib* was utilized, resulting in a visually appealing and well-organized arrangement of the plots. Finally, the show function from *matplotlib* was invoked to display the generated violin plots, enabling visual inspection and interpretation of the morphological differences between Melanocytes and SK-MEL-28 cells. This comprehensive data analysis pipeline, encompassing data loading, preprocessing, visualization, and plot customization, provides a robust and reproducible approach to comparing and understanding the distribution of morphological features across different cell types. The resulting violin plots offer valuable insights into the distinct patterns and characteristics exhibited by Melanocytes and SK-MEL-28 cells, facilitating further biological interpretation and hypothesis generation.

2.5. Hierarchical clustering and Heatmap Visualization of the correlation matrix

This article is protected by copyright. All rights reserved.

Author Manuscript

The dataset used in this study consists of multiple parameters measured across different samples. Preprocessing steps were undertaken to ensure data integrity and consistency. In order to understand the relationships between different parameters, a correlation matrix was calculated using the Pearson correlation coefficient, which measures the linear relationship between pairs of variables. Hierarchical clustering was performed on the correlation matrix to identify groups exhibiting similar parameters. This clustering method constructs a hierarchy of clusters and was applied using the complete linkage method, which considers the maximum distance between points in different clusters. The distance metric used was based on the Pearson correlation coefficient. To visualize this data, a heatmap was created with the pheatmap package in R. The heatmap utilized a color scheme encompassing from blue (negative correlations) to red (positive correlations), with white representing no correlation. Parameter names were annotated on both axes, with label font sizes adjusted for readability.

2.6. Measurement of Cell Area, Volume, and Diameter

The measurements were taken at 12-hour intervals over a period of 36 hours (0, 12, 24, and 36 hours). Each time point included three biological replicates for both Melanocytes and SK-MEL-28 cells. The mean cell area was calculated by the HoloMonitor M4 software, which automatically segments and measures the area of individual cells in the captured holographic images. The area was reported in square micrometers (μm^2). The mean cell volume was calculated using the HoloMonitor M4 software, which reconstructs the three-dimensional shape of each cell from the holographic images. The volume was reported in cubic micrometers (μm^3). The mean cell diameter was derived from the measured cell area and volume. The HoloMonitor M4 software calculates the diameter by assuming a spherical shape for the cells and using the formula for the volume of a sphere. The results were visualized using bar plots with error bars representing the standard deviation. The bar graphs were generated using the ggplot2 package in R, with additional enhancements for visual appeal

This article is protected by copyright. All rights reserved.

Author Manuscript

using the ggthemes package. The following steps were taken to create the bar graphs: the mean values and standard deviations for cell area, volume, and diameter were calculated for each time point and cell type. Bar plots were created for each parameter (area, volume, and diameter) with the x-axis representing the time points and the y-axis representing the measured values. Different colors were used to distinguish between Melanocytes and SK-MEL-28 cells. Error bars were added to the bar plots to represent the standard deviation of the measurements. Mean values were annotated on the bar plots to facilitate interpretation. The plots were enhanced using the ggthemes package to improve visual appeal, including custom color palettes and advanced themes.

Holographic microscopy estimates cell thickness by analyzing the phase shift induced by the passage of laser light through cells. This technique involves dividing a laser beam into reference and object beams, with the latter passing through the cell sample[25]. The interaction between the two beams creates an interference pattern, or hologram, which is recorded and processed to produce a phase image. The phase shift in this image is directly related to the optical properties and morphology of the cell. The maximum cell thickness is calculated from the phase shift, the refractive index of the cell, and the refractive index of the surrounding medium. In our study, we used default values for the refractive index of the cell 1.38 and the refractive index of the surrounding medium 1.34, which are based on literature reports [26, 27]. However, we acknowledge that variations in the refractive index can occur depending on cell type due to complexities of cell membrane structure, physiological state, and treatment conditions, as discussed in previous studies [28-30]. These variations introduce uncertainty into the calculated thickness values, as phase shifts can result from changes in either the refractive index or cellular morphology. To mitigate this, future studies could benefit from directly measuring the refractive index of each sample or applying correction factors for specific cell conditions. This approach might reduce variability and improve the accuracy of our cell thickness estimations. Future work should also explore advanced techniques for

This article is protected by copyright. All rights reserved.

Author Manuscript

refractive index measurement to enhance the precision of these holographic-based thickness calculations, especially under varying experimental conditions.

2.7. Cell Movement Plot

In order to identify patterns of cell movement over time between Melanocytes and SK-MEL-28 cells, we visualized the movement of the cells in their respective wells on a Cell Movement Plot. The analysis was completed using the App Suite Cell Imaging software of the HoloMonitor M4. Using the “In-Depth Analysis: Single Cell Tracking” package of the software, we analyzed 235 frames of the wells containing viable cells, which were taken at 15-minute intervals, via the “Identify Cells” function. These frames were then applied to the “Single Cell Tracking” function and integrated into an analysis to track cell movements across a 58-hour period. We opted to include every cell in the well under the "Cell Movement Plot" feature, thus ensuring that each cell was incorporated into the plot. In turn, a Cell Movement Plot with the movement of every cell was generated. Each line represents an individual cell track, and each cell is represented with a different colored line. The origin represents the cell’s original position, and movement across the x-axis indicates lateral movement from this original position (μm); movement across the y-axis indicates vertical movement from this original position (μm).

2.8. Heterogeneity analysis

The dataset for this study contained measurements of various morphological and optical properties of the melanoma cell lines SK-MEL-2 and SK-MEL-28. The data was imported into R for analysis, with missing values addressed by removing rows with incomplete data. Feature selection was performed using a Random Forest classification model, implemented with the caret package in R and validated through 5-fold cross-validation. Feature importance was assessed using the varImp function, and the most significant features were selected for further

This article is protected by copyright. All rights reserved.

Author Manuscript

analysis. A Mann-Whitney U test was conducted to evaluate the statistical significance of differences between the two cell lines, as this non-parametric test is well-suited for non-normal distributions. The wilcox.test function in R was used, with features having the lowest p-values identified as statistically significant.

Additionally, a heterogeneity index, calculated as the variance of each feature, was computed using the var function to assess variability within the cell populations. Key visualizations were created to illustrate these differences, including box plots of the top six important features using ggplot2 and a correlation heatmap for the top ten features using the heatmap function. All analyses and visualizations were performed in R (version 4.0.0) using the packages caret, dplyr, tidyr, ggplot2, and stats, within a Jupyter Notebook environment to allow for interactive exploration and comprehensive documentation of the results.

2.9. **Data evaluation and visualization**

The data was evaluated and visualized utilizing Python 3.12.1 and R 4.3.3. In Python, the following libraries were utilized: scikit-learn for data standardization and principal component analysis (PCA), matplotlib for creating various plots, including scatter plots for PCA and t-distributed stochastic neighbor embedding (t-SNE), seaborn for generating violin plots, pandas for data manipulation and analysis, and numpy for numerical operations. In R, the ggplot2 and ggthemes packages were used for creating and customizing bar plots, pheatmap for heatmap visualization, and dplyr and tidyr for data manipulation and tidying. Statistical analysis was performed using the stats package, and machine learning models were implemented with the caret package.

2.10. Statistical Analysis

The morphological data of normal melanocytes and SK-MEL-28 melanoma cells were pre-processed to ensure accuracy and reliability. Data normalization was performed during the Principal Component Analysis (PCA) step, where each feature was centered and

This article is protected by copyright. All rights reserved.

Author Manuscript

scaled. Outliers were evaluated, and infinite values were replaced with NA, with rows containing NA values subsequently removed from the dataset. The data are presented as mean ± standard deviation (SD) to provide a clear understanding of the variability within each group. The sample size for each cell type was as follows: normal melanocytes (n = 10,114) and SK-MEL-28 melanoma cells (n = 10,844). To assess significant differences in morphological features between the two cell types, a multivariate analysis of variance (MANOVA) was performed. This two-sided test was chosen to evaluate overall differences across multiple dependent variables simultaneously, with the significance level set at an alpha value of 0.05. Post-hoc analyses were conducted using Bonferroni-corrected t-tests to identify specific features contributing to the observed differences. Assumptions of normality and homogeneity of variance were evaluated and met for the chosen tests. All statistical analyses were performed using R software with the 'ggplot2' package used for data visualization and 'Rtsne' for t-SNE analysis.

Violin plot analysis was directly conducted without any additional transformation or normalization, as the focus was on visualizing the raw distribution of the numeric features. Outliers were retained to provide a complete view of the data distribution, including any potential anomalies. The violin plots were used to present the distribution of each morphological feature across various groups, showing data density and variability. The analysis included a sample size of 20,961 data points, with missing or infinite values removed. The primary statistical method employed was violin plots, which combined the features of boxplots and kernel density plots to give a detailed view of the data distribution. No significance tests were conducted, as the focus was on exploratory visualization. The analysis was performed using R, with packages such as readxl, dplyr, ggplot2, and reshape2 to manipulate and visualize the data effectively.

For the clustered heatmap of the correlation matrix, the data was initially loaded from an Excel file and filtered to include only relevant groups (SK-MEL-28 and Melanocytes). No

This article is protected by copyright. All rights reserved.

Author Manuscript

transformations or normalizations were applied before calculating the correlation matrix. Outliers were not explicitly addressed, and missing values were handled by excluding incomplete observations from the correlation computation. The correlation matrix was visualized using a clustered heatmap to provide insights into the relationships between various morphological features. The exact sample size for each group was based on the data available in the Excel sheet. Pearson correlation coefficients were calculated to assess the linear relationships between features, though no hypothesis testing was conducted, and there were no associated alpha or p-values. The analysis was conducted using R, with the readxl package for data loading, pheatmap for heatmap visualization, and base R functions for computing the correlation matrix.

3. Results

3.8. Distinct Morphological Differences Between Melanocytes and SK-MEL-28 Cells Revealed by 2D and 3D Microscopy

2D and pseudo 3D Microscopy of the Melanocytes and SK-MEL-28 cells revealed distinct morphological properties between the two cell lines, including area, optical volume, and thickness. The 2D microscope images revealed overt characteristic differences between Melanocytes and SK-MEL-28 cells from an overhead view. As represented in Figure 1A, the Melanocytes were characterized by elongated, irregular shapes with convex boundaries; that is, the perimeter of the Melanocytes greatly deviated from the circumference of a perfect circle. The SK-MEL-28 cells were characterized by elongated, convex boundaries as well; however, they displayed more regular, circular boundaries in contrast to the Melanocytes. These observations suggest the presence of distinct morphological differences between Melanocytes and SK-MEL-28 cells, which reveals their potential to be used as distinguishing characteristics.

This article is protected by copyright. All rights reserved.

Author Manuscript

Furthermore, the pseudo 3D microscope images of the Melanocytes and SK-MEL-28 cells revealed more covert property differences between individual cells, including differences in thickness, length, and width (Figure 1B). The Melanocyte under observation exhibited a cell length of 85 μm and a cell width of 13 μm, corroborating the observations from the 2D microscopy regarding its elongated, irregular shape. In contrast, the SK-MEL-28 cell under observation exhibited a cell length of 81 μm and a cell width of 23 μm, corroborating the observations from the 2D microscopy regarding its elongated, more regular shape. Moreover, from the pseudo 3D plots, it was found that the Melanocyte peak was 6.8 μm and the SK-MEL-28 cell peak was found to be 8.4 μm. Melanocytes overall had lower values for optical thickness in contrast to the SK-MEL-28 cells, suggesting distinctions with regard to thickness between the two cell lines.

Overall, these findings visualize distinct morphological differences between Melanocytes and SK-MEL-28 cells, as the Melanocytes were observed to have more irregular shapes and lower optical thickness in contrast to the SK-MEL-28 cells. However, both Melanocytes and SK-MEL-28 cells had convex boundaries with elongated shapes. These findings in terms of visual differences could be used to further distinguish between the two cell lines.

3.9. Distinct Morphological Clustering of Melanocytes and SK-MEL-28 Cells Revealed by PCA and t-SNE Analysis

This article is protected by copyright. All rights reserved.

Author Manuscript

The PCA of the morphological features of Melanocytes and SK-MEL-28 cells revealed distinct clustering patterns between the two cell types. The PCA plot, which reduced the high-dimensional morphological data to two principal components, effectively captured the variance in the dataset and provided a clear visual separation between the groups. In the PCA plot (Figure 2A), Melanocytes were represented in black, while SK-MEL-28 cells were represented in red. The first principal component (PC1) and the second principal component (PC2) accounted for the majority of the variance in the data, allowing for a two-dimensional visualization. The plot demonstrated that Melanocytes and SK-MEL-28 cells occupy distinct regions in the principal component space, indicating significant differences in their morphological characteristics. The clustering of Melanocytes in one region and SK-MEL-28 cells in another suggests that the PCA successfully captured the inherent morphological differences between the two cell types. This separation highlights the effectiveness of PCA in distinguishing between cell types based on their morphological features.

The t-SNE plot of the morphological features of Melanocytes and SK-MEL-28 cells revealed distinct clustering patterns and separation between the two cell types in the reduced-dimensional space (Figure 2B). The plot, generated using a two-dimensional t-SNE projection, effectively captured the underlying structure and differences in the high-dimensional morphological data. Melanocytes formed a tight and compact cluster in one region of the plot, indicating a high degree of similarity in their morphological characteristics. In contrast, SK-MEL-28 cells clustered separately from Melanocytes, occupying a distinct region in the t-SNE space. The clear separation between the two cell types suggests that their morphological features are significantly different and can be used to distinguish between them. The t-SNE plot also revealed potential substructures within each cell type cluster. Melanocytes exhibited a more homogeneous distribution, with minimal dispersion, implying a consistent morphological profile among the samples. In contrast, SK-MEL-28 cells displayed a slightly more dispersed pattern, suggesting a higher level of morphological heterogeneity within this cell type. The centroid coordinates provided a quantitative measure of the separation between

This article is protected by copyright. All rights reserved.

Author Manuscript

the two cell types in the t-SNE space. The distinct centroid locations further supported the visual observation of clear clustering and differentiation between Melanocytes and SK-MEL-28 cells based on their morphological features.

3.10. SK-MEL-28 Cells Exhibit Greater Size Variability and Distinct Optical Properties Compared to Melanocytes

The violin plots generated from the morphological feature data provide a comprehensive visual comparison of the distribution and characteristics of Melanocytes and SK-MEL-28 cells. The analysis reveals distinct differences between the two cell types across various morphological aspects. For the features of Area, Boxed breadth, and Boxed length, the violin plots demonstrate that Melanocytes generally have smaller values compared to SK-MEL-28 cells (Figure 3A-C). The distribution of these features for Melanocytes is more concentrated towards lower values, indicating that Melanocytes tend to have smaller cell areas and dimensions. In contrast, SK-MEL-28 cells exhibit a wider range of values for these features, suggesting greater variability in their size and shape.

The violin plots for Eccentricity, Hull convexity, and Irregularity highlight notable differences in cell shape and regularity between the two cell types (Figure 3D-F). Melanocytes display higher overall values for Irregularity compared to SK-MEL-28 cells, suggesting that Melanocytes have a more irregular shape and SK-MEL-28 cells have a more regular shape. Both Melanocytes and SK-MEL-28 cells had similar averages and overall distribution with respect to Eccentricity and Hull Convexity, suggesting that both cell lines had elongated shapes with similarly convex boundaries.

Regarding the optical properties, the violin plots for Optical volume, Perimeter length, and Shape convexity reveal distinct patterns (Figure 3G-I). Melanocytes have smaller optical volumes and shorter perimeter lengths compared to SK-MEL-28 cells, suggesting differences

This article is protected by copyright. All rights reserved.

Author Manuscript

in their overall size and surface area. Additionally, SK-MEL-28 cells exhibit higher Shape convexity values, indicating a more compact and convex shape compared to Melanocytes. The violin plots for Average optical path length, Max optical path length, Average optical thickness, and Max optical thickness further highlight the differences in optical characteristics between the two cell types (Figure 3J-M). Melanocytes consistently show lower values for these features, suggesting that they have shorter optical path lengths and thinner optical profiles compared to SK-MEL-28 cells. These differences in optical properties may reflect variations in the internal structure and composition of the cells.

The mean values for each morphological feature and cell type provide a quantitative comparison between Melanocytes and SK-MEL-28 cells as shown in Table 1. These mean values confirm the observations from the violin plots and provide a numerical summary of the differences between the two cell types. For the features of Area, Boxed breadth, and Boxed length, SK-MEL-28 cells have higher mean values compared to Melanocytes, indicating that SK-MEL-28 cells are generally larger in size and dimensions. The mean values for Eccentricity and Hull convexity are similar between the two cell types, suggesting that the overall shape and convexity of the cells are comparable. However, SK-MEL-28 cells have a lower mean value for Irregularity, indicating a more regular shape compared to Melanocytes. Regarding optical properties, SK-MEL-28 cells exhibit higher mean values for Optical volume and Perimeter length, confirming their larger size and surface area. The mean value for Shape convexity is higher in SK-MEL-28 cells, suggesting a more convex and uneven shape compared to Melanocytes. The mean values for Average optical path length, Max optical path length, Average optical thickness, and Max optical thickness are consistently higher in SK-MEL-28 cells, indicating that they have longer optical path lengths and thicker optical profiles compared to Melanocytes.

This article is protected by copyright. All rights reserved.

Author Manuscript

These quantitative comparisons provide a clear and concise summary of the morphological differences between Melanocytes and SK-MEL-28 cells, complementing the visual insights gained from the violin plots.

3.11. Violin Plot Analysis Shows Comparable Spatial Characteristics for Melanocytes and SK-MEL-28 Cells with Subtle Differences in Peak Positions

The violin plots for the positional and geometric parameters provide additional insights into the spatial characteristics of Melanocytes and SK-MEL-28 cells. These parameters include Boxed center position X and Y, Centroid position X and Y, and Peak position X and Y (Figure 4A-F). For Boxed center position X and Y, the violin plots reveal varied distributions between Melanocytes and SK-MEL-28 cells. The overlapping distributions suggest that the position of the bounding box center is not significantly different between the two cell types, though the average values for each position vary. This indicates that the overall spatial positioning of the cells within their bounding boxes is comparable. Similarly, the violin plots for Centroid position X and Y show overlapping distributions between Melanocytes and SK-MEL-28 cells, though the overall distribution and average values for SK-MEL-28 cells display higher values. The centroid position represents the center of mass of the cell, and the similarity in distributions suggests that the spatial location of the cell centroids is not substantially different between the two cell types. Similarly, the violin plots for Peak position X and Y reveal slight differences in the distribution of peak positions between Melanocytes and SK-MEL-28 cells. The peak position corresponds to the location of the highest point or intensity within the cell. The violin plots indicate that the peak positions for Melanocytes are more concentrated towards the center of the distribution, while SK-MEL-28 cells exhibit a wider spread in peak positions. This suggests that there may be some variations in the spatial distribution of peak intensities between the two cell types.

This article is protected by copyright. All rights reserved.

Author Manuscript

The mean values for each positional and geometric feature and cell type provide a quantitative comparison between Melanocytes and SK-MEL-28 cells, shown in Table 1. These mean values complement the observations from the violin plots and offer a numerical summary of the positional and geometric differences between the two cell types. For Boxed center position X and Y, the mean values are relatively similar between Melanocytes and SK-MEL-28 cells, confirming the overlapping distributions observed in the violin plots. This suggests that the average position of the bounding box center is comparable for both cell types. Similarly, the mean values for Centroid position X and Y are close between Melanocytes and SK-MEL-28 cells, indicating that the average position of the cell's center of mass is not significantly different between the two cell types. Specifically, the SK-MEL-28 cells have higher average Centroid position values, though their distribution is varied. The mean values for Peak position X and Y show some differences between Melanocytes and SK-MEL-28 cells. The mean peak position for Melanocytes is slightly closer to the center of the distribution compared to SK-MEL-28 cells, which aligns with the observations from the violin plots. Given the geometric center (Boxed Center positions), center of mass (Centroid positions), and Peak Positions exhibit similarities, it is suggested that the nuclei of the cell lines reside at these relative positions. These quantitative comparisons provide a concise summary of the positional and geometric differences between Melanocytes and SK-MEL-28 cells, supporting the insights gained from the violin plots. Overall, the analysis of positional and geometric parameters reveals that while there are some subtle differences in peak positions, the overall spatial characteristics of Melanocytes and SK-MEL-28 cells are relatively comparable in terms of bounding box center and centroid positions.

3.12. **Phase Shift Parameters Distinguish Melanocytes from SK-MEL-28 Cells with Higher Values and Variability**

The violin plots for Phase Shift Parameters reveal significant differences between Melanocytes and SK-MEL-28 cells. These visualizations provide a clear and informative

This article is protected by copyright. All rights reserved.

Author Manuscript

comparison of the distribution and characteristics of the two cell types across various phase shift measures, which could be used to estimate cell thickness and volume. For Phase shift average, the violin plot demonstrates that SK-MEL-28 cells exhibit consistently higher values compared to Melanocytes (Figure 5A). The distribution of this parameter for SK-MEL-28 cells is shifted towards the upper range, indicating that these cells have greater phase shift values. In contrast, Melanocytes show lower values and distributions concentrated towards the lower range.

Similarly, the violin plots for Phase shift standard deviation and sum highlight notable differences between the two cell types (Figure 5B-C). SK-MEL-28 cells display wider distributions and higher values for both parameters, suggesting greater variability and overall magnitude of phase shift compared to Melanocytes. The broader spread of the distributions for SK-MEL-28 cells indicates a more diverse range of phase shift values within this cell type. These violin plots provide a visually compelling representation of the distinct phase shift characteristics of Melanocytes and SK-MEL-28 cells. The clear separation and differences in the distributions underscore the potential of Phase Shift Parameters as valuable indicators for distinguishing between these cell types and understanding their unique cellular properties.

The visualizations complement the quantitative analysis of mean values indicated in Table 1, reinforcing the findings that SK-MEL-28 cells exhibit significantly higher values and greater variability in Phase Shift Parameters compared to Melanocytes. In conclusion, the violin plots for Phase Shift Parameters offer a powerful visual tool for comparing and contrasting the phase shift characteristics of Melanocytes and SK-MEL-28 cells. The results highlight the distinct differences between the two cell types and emphasize the potential of these parameters as biomarkers for cell characterization and differentiation.

3.13. Melanocytes Exhibit Greater Surface Roughness Than SK-MEL-28 Cells

This article is protected by copyright. All rights reserved.

Author Manuscript

To investigate the differences in surface roughness characteristics between Melanocytes and SK-MEL-28 cells, we analyzed Roughness average (Figure 5D). A violin plot was generated to visualize the distribution of this parameter for each cell type, which reveals distinct differences between Melanocytes and SK-MEL-28 cells. Melanocytes exhibit higher values for Roughness average compared to SK-MEL-28 cells, indicating a greater degree of surface roughness on average.

The difference in distribution indicated by the violin plot is corroborated by the mean values for average Roughness as listed in Table 1. These findings underscore the potential of Roughness Parameters as valuable indicators for distinguishing between Melanocytes and SK-MEL-28 cells based on their surface roughness characteristics. The observed differences may have implications for cellular processes and warrant further investigation into their biological significance and potential applications in cell characterization and classification.

3.14. Texture Parameter Analysis Highlights Higher Contrast and Entropy in Melanocytes Compared to SK-MEL-28 Cells

Texture Parameters were analyzed to investigate the differences between Melanocytes and SK-MEL-28 cells. The analysis focused on three sets of Texture Parameters: Texture clustershade, Texture cluster tendency, and Texture contrast (Figure 6A-C); Texture correlation (Figure 6D); and Texture energy, Texture entropy, Texture max probability, and Texture homogeneity (Figure 6E-H).

Violin plots were generated to visualize the distribution of each Texture Parameter for both cell types. The plots revealed distinct differences in the distribution of Texture Parameters between Melanocytes and SK-MEL-28 cells. Melanocytes exhibited higher values and wider distributions for Texture clustershade, Texture contrast, and Texture entropy compared to SK-MEL-28 cells. Given Texture clustershade refers to the image symmetry, it is suggested that the Melanocytes exhibited a less symmetrical image due to its higher value. Additionally, it is

This article is protected by copyright. All rights reserved.

Author Manuscript

suggested that there is a greater degree of depth variation in the Melanocyte surface, given texture contrast measures the thickness contrast between the pixels of the cell image, as well as a greater nonuniformity and complexity, as indicated by the Texture entropy. In contrast, SK-MEL-28 cells showed higher values and wider distributions for Texture homogeneity, Texture correlation, Texture energy, and Texture clustertendency. The higher values for these parameters indicate a greater texture consistency, uniformity, and non-randomness in contrast to the Melanocytes.

The plots did, however, reveal similarities between SK-MEL-28 cells and Melanocytes in Texture max probability. The analysis of Texture Parameters reveals distinct differences between Melanocytes and SK-MEL-28 cells. The violin plots, mean value comparisons, and statistical tests consistently demonstrate that Melanocytes exhibit higher values for Texture clustershade, Texture contrast, and Texture entropy, while SK-MEL-28 cells show higher values for Texture homogeneity, Texture correlation, Texture energy, and Texture Clustertendency. These values suggest a varying cell texture between Melanocytes and SK-MEL-28 cells, with the Melanocytes exhibiting greater asymmetry and heterogeneity in contrast to the SK-MEL-28 cells.

The mean values of each Texture parameter provide a quantitative approach to the trends illustrated in the Violin Plots (Table 1). These findings highlight the potential of Texture Parameters as valuable indicators for cell characterization and classification.

3.15. **Clustered Heatmap Analysis Reveals Strong Correlations Between Key Parameters**

The correlation matrix was computed to examine the linear relationships between the various parameters in the dataset (Figure 7). The Pearson correlation coefficients ranged from -1 to 1, indicating the strength and direction of these relationships, with positive values indicating a

This article is protected by copyright. All rights reserved.

Author Manuscript

direct relationship and negative values indicating an inverse relationship. To visualize the correlation matrix and identify clusters of highly correlated parameters, a clustered heatmap was generated using hierarchical clustering. This method grouped similar parameters together based on their correlation coefficients, with dendrograms on the rows and columns representing the hierarchical clustering structure. The heatmap revealed several distinct clusters of parameters with high correlations, visually represented by blocks of similar colors along the diagonal. The color gradient ranged from blue to red, indicating the strength of the correlations, with blue representing negative correlations, white representing no correlation, and red representing positive correlations. Hierarchical clustering effectively grouped parameters with similar correlation patterns, facilitating the identification of relationships and potential interactions between parameters. The smaller font size for the labels ensured visibility of all parameter names despite the large number of variables.

Strong positive correlations were observed between several parameters. For example, 'Avg. Area (pxl)' and 'Avg. Area (μm²)' exhibited a perfect correlation of 1.0, as they are different units of the same measurement. Similarly, 'Avg. Boxed breadth (pxl)' and 'Avg. Boxed breadth (μm)' also had a perfect correlation of 1.0 for the same reason. Additionally, 'Avg. Area (pxl)' and 'Avg. Boxed breadth (pxl)' showed a very high correlation of approximately 0.986, indicating that larger areas tend to have larger breadths. On the other hand, notable negative correlations included 'Avg. Boxed center pos Y (pxl)' and 'Avg. Area (pxl)', which had a strong negative correlation of approximately -0.729, suggesting that as the area increases, the Y position of the boxed center tends to decrease.

To investigate the biological or physical significance of specific clusters identified in the heatmap, the following steps were taken: First, the clusters were extracted from the hierarchical clustering results. Next, the parameters within each cluster were analyzed to understand their potential biological or physical significance. Finally, these parameters were cross-referenced with existing literature or databases to validate their significance. For

This article is protected by copyright. All rights reserved.

Author Manuscript

instance, one cluster included the parameter 'No. tracked cells', which is fundamental in cell tracking studies and provides insights into cell proliferation and migration. Another cluster contained area and breadth measurements such as 'Avg. Area (pxl)', 'Avg. Area (μm²)', 'Avg. Boxed breadth (pxl)', 'Avg. Boxed breadth (μm)', and 'Avg. Boxed center pos X (pxl)'. These parameters are crucial for understanding cell size, growth, shape, and morphology. Cross-referencing with literature validated the significance of these clusters, highlighting their relevance in studies on cell tracking, size regulation, and morphological changes. The clustered heatmap provided valuable insights into the data structure, highlighting closely related parameter groups. In turn, these correlations can be used to investigate underlying mechanisms and inform subsequent analyses.

3.16. Differences in Mean Cell Area, Volume, and Diameter Over Time

Melanocytes and SK-MEL-28 mean cell area, mean cell volume, and mean cell diameter data were collected at 12-hour intervals, with results depicted in Figure 8. The measurements showed significant differences between the two cell types over time. The mean cell area for Melanocytes started at 513.50 μm² at hour 0 and showed a slight decrease to 492.0 μm² by hour 48 (Figure 8A). For SK-MEL-28, the mean cell area started at 643.0 μm² at hour 0 and decreased to 612.0 μm² by hour 48. The error bars represent the standard deviation of the measurements, indicating the variability within the samples. The data suggests that both cell types exhibit a decrease in mean cell area over time, with SK-MEL-28 cells consistently having a larger mean cell area compared to Melanocytes. The mean cell volume for Melanocytes started at 1,100.0 μm³ at hour 0 and increased to 1,220.0 μm³ by hour 48 (Figure 8B), indicating a relatively consistent mean cell volume over time. For SK-MEL-28, the mean cell volume started at 2,190.0 μm³ at hour 0 and increased to 2,310.0 μm³ by hour 48. The error bars represent the standard deviation of the measurements. The data indicates that both cell types exhibit an increase in mean cell volume over time, with SK-MEL-28 cells having a consistently larger mean cell volume and mean cell volume increase compared to

This article is protected by copyright. All rights reserved.

Author Manuscript

Melanocytes. The mean cell diameter for Melanocytes started at 25.32 μm at hour 0 and decreased to 24.8 μm by hour 48 (Figure 8C). For SK-MEL-28, the mean cell diameter started at 27.7 μm at hour 0 and decreased to 27.2 μm by hour 48. The error bars represent the standard deviation of the measurements. The data indicates that both cell types exhibit a decrease in mean cell diameter over time, with SK-MEL-28 cells having a consistently larger mean cell diameter compared to Melanocytes.

3.17. SK-MEL-28 Cells Exhibit More Varied Movement Compared to Melanocytes

The Cell Movement Plot was used to analyze overall cell movement patterns and directionality between Melanocytes and SK-MEL-28 cells (Figure 9). The origin (0,0) represents a normalized beginning position for each cell analyzed, and the x- and y-axes indicate movement along each axis, respectively. Each colored line denotes the migration of a single cell in the well measured. The Cell Movement Plots reveal differences in overall cell migration patterns between the Melanocytes and SK-MEL-28 cells. As represented in Figure 9A, the Melanocytes remained relatively close to their point of origin and tended to move in one direction.

On the other hand, as represented in Figure 9B, the overall SK-MEL-28 cell movement was more varied and asymmetric, with more scattered movement along the y-axis compared to the x-axis. In addition, the SK-MEL-28 Cell Movement Plot displays that the SK-MEL-28 cells were more likely to travel greater distances from the origin compared to the Melanocytes, as revealed by the more distant tracks from the origin.

These findings suggest that there are apparent differences between Melanocytes and SK-MEL-28 cells in terms of directional cell migration: the SK-MEL-28 cells were more likely to travel to distances further from their place of origin with more asymmetric movement patterns as compared to the Melanocytes. They indicate the possibility of using cell migration as a parameter in distinguishing between Melanocytes and SK-MEL-28 cells.

This article is protected by copyright. All rights reserved.

Author Manuscript

3.18. Distinctive Features of SK-MEL-2 and SK-MEL-28 Cell Lines

Our analysis of the SK-MEL-2 and SK-MEL-28 melanoma cell lines revealed significant differences in their morphological and optical properties. The Random Forest model identified key features such as Peak pos Y (pxl), Boxed center pos Y (pxl), and Centroid pos Y (μm) as the most important for distinguishing between the cell lines (Figure 10). Statistical analysis using the Mann-Whitney U test confirmed these findings, with the lowest p-values observed for Y-position features, indicating significant differences between the cell lines. The heterogeneity index analysis showed that SK-MEL-2 cells exhibited greater variability in features like Optical volume (μm^3) and Area (μm^2) compared to SK-MEL-28 cells. Visualizations, including box plots (Figure 10, A) and a correlation heatmap (Figure 10B), further illustrated these differences, highlighting the distinct spatial and optical characteristics of the two cell lines. These findings provide valuable insights into the heterogeneity and distinguishing features of SK-MEL-2 and SK-MEL-28, with potential implications for melanoma research and therapeutic development.

4. Discussion

Quantitative phase imaging (QPI) has become a formidable technique for characterizing cells without the need for labels, utilizing the principles of digital holographic microscopy (DHM) to offer comprehensive insights into cellular morphology and dynamics. In the last twenty years, there have been notable advancements in QPI methods, which have broadened their use in cell biology. Various QPI methodologies have been developed highlighting their dependability and quantitative mapping capabilities[31]. These advancements have streamlined the use of interference microscopy, making it more accessible for biological applications. Quantitative Phase-Digital Holographic Microscopy (QP-DHM) has the potential to non-invasively visualize

This article is protected by copyright. All rights reserved.

Author Manuscript

cellular structures and monitor dynamic processes, such as neuronal activity and spine dynamics, which are crucial for understanding cellular functions in neuroscience and psychiatry [32]. Additionally, advancements in QPI have shown how specific biophysical parameters can be extracted from quantitative phase signals, offering critical biological insights for cell characterization [33]. Despite these advances, challenges remain in interpreting quantitative phase signals in relation to biological processes. Accurately determining parameters such as absolute cell volume and membrane fluctuations is essential for furthering our understanding of cellular behavior [34]. This body of work addresses these challenges by employing advanced numerical algorithms to enhance the classification and characterization of cells based on their morphological and physical properties. The novelty of this approach is the integration of a commercial DHM QPI system with advanced numerical techniques, allowing for more accurate cell classification. By deriving specific biophysical parameters and correlating them with cellular functions contributes to the development of quantitative microscopy and opens new avenues for research in cell biology and related fields.

The results obtained from the study on the distinct morphological differences between Melanocytes and SK-MEL-28 cells using holographic microscopy revealed significant variations in the morphological properties of the two cell lines. The observations from the microscopy images indicated that Melanocytes exhibited elongated, irregular shapes with convex boundaries, while SK-MEL-28 cells displayed more regular, circular boundaries, suggesting distinct morphological differences between the two cell types, Figure 1A. Additionally, the pseudo 3D microscopy images highlighted differences in thickness, length, and width between individual cells, with Melanocytes showing lower optical thickness compared to SK-MEL-28 cells, Figure 1B.

The results from the morphological clustering analysis using PCA and t-SNE techniques further supported the distinct differences between Melanocytes and SK-MEL-28 cells (Figure

This article is protected by copyright. All rights reserved.

Author Manuscript

2). The PCA plot clearly separated the two cell types based on their morphological characteristics, with Melanocytes and SK-MEL-28 cells occupying distinct regions in the principal component space, indicating significant differences in their morphological features. Similarly, the t-SNE plot revealed clear clustering patterns and separation between the two cell types, emphasizing the significant differences in their morphological profiles. Moreover, the violin plot analysis provided a comprehensive comparison of the distribution and characteristics of Melanocytes and SK-MEL-28 cells across various morphological aspects (Figure 3). The analysis highlighted distinct differences in cell size, shape, and optical properties between the two cell lines, with SK-MEL-28 cells exhibiting greater sizes and distinct optical properties compared to Melanocytes. The mean values for each morphological feature further confirmed these differences, with SK-MEL-28 cells consistently showing higher values for area, volume, thickness, and other parameters compared to Melanocytes (Table 1). The morphological parameters of area, volume, and diameter were further corroborated by temporal bar graphs that revealed a consistently higher mean area, volume, and diameter for SK-MEL-28 cells in contrast to Melanocytes over time (Figure 8). Morphological features regarding cell shape also revealed distinct patterns: Melanocytes displayed higher Irregularity values than SK-MEL-28 cells, indicating a more irregular shape, but similar Eccentricity values, suggesting both cell lines have elongated shapes.

Other studies have focused separately on the morphology of melanocytes and SK-MEL-28 cells, though, to our knowledge, they have not been directly compared. Previous research has identified that SK-MEL-28 cells exhibit polygonal morphology

[35], as well as a mixture of triangular dendritic and elongated dendritic morphologies [36]. Similarly, in our study, SK-MEL-28 cells exhibited irregular, elongated shapes with more rounded boundaries. Additionally, it has been found that melanocyte morphology varies with age, becoming “larger, more dendritic” as age increases [37]. These findings regarding

This article is protected by copyright. All rights reserved.

Author Manuscript

changes in melanocyte morphology raise a question for future studies regarding differences in melanoma morphology in patients of different ages, comparing it to changes in melanocyte morphology. Such studies would further elucidate the overall characteristics of melanoma.

Additionally, the analysis of positional and geometric parameters revealed subtle differences in peak positions between Melanocytes and SK-MEL-28 cells, while overall spatial characteristics remained comparable (Figure 4). Furthermore, the study delved into phase shift parameters, surface roughness, and texture analysis to further differentiate between Melanocytes and SK-MEL-28 cells. The phase shift parameters indicated that SK-MEL-28 cells exhibited higher values and greater variability compared to Melanocytes, suggesting distinct optical characteristics between the two cell types (Figure 5A-C). Moreover, the analysis of surface roughness revealed that Melanocytes exhibited greater surface roughness compared to SK-MEL-28 cells, indicating differences in the texture of the cell surfaces (Figure 5D). Texture parameter analysis highlighted higher contrast and entropy in Melanocytes compared to SK-MEL-28 cells, indicating greater texture heterogeneity and nonuniformity in Melanocytes. These findings further emphasize the unique textural features of the two cell lines (Figure 6).

Furthermore, as demonstrated in Figure 7, the clustered heatmap of correlation revealed strong positive and negative correlations between several parameters. Such groupings may assist with the identification of crucial relationships between parameters. Moreover, the Cell Movement Plots revealed differences in cell migration directionality, whereas SK-MEL-28 cells exhibited more scattered, varied movement in comparison to Melanocytes (Figure 9).

This article is protected by copyright. All rights reserved.

Author Manuscript

Heterogeneity analysis between two melanoma cell lines, SK-MEL-28 and SK-MEL-2 (Figure 10), reveal a distinct separation observed in Y-position features, including Peak pos Y (pxl), Boxed center pos Y (pxl), and Centroid pos Y (μm). This data highlights the significant differences between the two cell lines, as identified by both the Random Forest model and the Mann-Whitney U test. These Y-position features are critical in distinguishing between SK-MEL-2 and SK-MEL-28, (Figure 10 A). Furthermore, the box plots indicate that SK-MEL-2 cells exhibit a wider distribution in features such as Optical volume (μm^3), suggesting greater heterogeneity within this cell line. This observed variability may reflect underlying biological differences that could influence both the behavior and therapeutic response of SK-MEL-2 cells.

Figure 10B complements these findings with a correlation heatmap, which highlights the relationships between the top distinguishing features. The strong positive correlations among Y-position features suggest a consistent pattern across multiple measurement methods, further emphasizing their relevance in distinguishing the cell lines. Additionally, moderate correlations between Optical volume and other features reflect the complex, multifaceted nature of cell morphology and optical properties. Notably, features such as Texture clustertendency exhibit weak correlations with other parameters, indicating their potential as independent contributors to the observed cellular differences and warranting further exploration.

Collectively, these visual analyses provide important insights into the distinct spatial and optical characteristics of the SK-MEL-2 and SK-MEL-28 cell lines. The increased heterogeneity observed in SK-MEL-2, particularly in terms of Optical volume and Area, may

This article is protected by copyright. All rights reserved.

Author Manuscript

have significant implications for understanding melanoma heterogeneity and informing the development of targeted therapies. These findings underscore the value of integrating statistical analysis, and advanced visualization techniques to uncover meaningful patterns in complex biological datasets, with the potential to enhance melanoma research and therapeutic strategies.

Our study shares several similarities with prior research, particularly in the use of label-free imaging techniques and machine learning algorithms for cancer cell characterization [38, 39]. Utilization of label-free methods to avoid chemical staining or labeling aids in preserving the natural state of cells during imaging. Similarly, our work adopts a label-free approach, allowing us to achieve more accurate morphological analysis without altering cell properties. This technique is crucial for maintaining the integrity of the cells' natural state. [39, 40]include the shared focus on cancer cell characterization. Previous studies have emphasized the identification and classification of various cancer types, such as circulating tumor cells (CTCs) and tumor subtypes and analyzed cell morphology [38, 40]. Our research similarly aims to differentiate melanoma cells from melanocytes, contributing to a deeper understanding of cancer cell behavior and opening up potential avenues for improved cancer diagnostics and treatment monitoring.

Despite these similarities, our approach advances the field in several key areas. One significant difference is in the imaging methodology and analysis. While previous studies, employed Quantitative Phase Imaging (QPI) and Digital Holographic Microscopy (DHM) for imaging, our work integrates advanced numerical algorithms for data analysis[39, 40]. This integration enhances the precision of cell classification and provides more detailed morphological information. To the best of our knowledge, our use of DHM, combined with

This article is protected by copyright. All rights reserved.

Author Manuscript

machine learning, allows for a more refined differentiation between melanoma and melanocytes, which has not been explored as thoroughly in earlier works. While previous studies[40, 41], demonstrated the ability to differentiate cancer cells from other cell types, such as blood cells, our work advances the field by focusing on the specific morphological and motility differences between melanoma cells and melanocytes. This targeted analysis allows for more precise melanoma characterization and lays the groundwork for future non-invasive diagnostic methods. Although our study demonstrates promising results in melanoma characterization, further research is needed to validate the generalizability of our method across other cancer types. For instance, additional validation with different cell lines would build on the broader findings of previous studies [40, 41].

In conclusion, the comprehensive analysis of morphological differences, clustering patterns, size variability, optical properties, positional parameters, phase shift characteristics, surface roughness, and textural features provided a detailed understanding of the distinct morphological profiles of Melanocytes and SK-MEL-28 cells. Furthermore, heterogeneity analysis offers valuable insights into the distinct spatial and optical characteristics of SK-MEL-2 and SK-MEL-28 cell lines. The observed heterogeneity in SK-MEL-2 cells, particularly in terms of Optical volume and Area, may have implications for understanding melanoma heterogeneity and developing targeted therapies. These findings not only contribute to the characterization of these cell lines but also offer valuable insights into potential biomarkers for distinguishing between different cell types based on their morphological properties. The study underscores the importance of morphological analysis in cellular research and highlights the significance of advanced microscopy techniques and computational analyses in elucidating cellular differences.

This article is protected by copyright. All rights reserved.

Author Manuscript

Funding

This research was partially funded by the Summer Undergraduate Research Experience (SURE) at the University of Michigan-Dearborn, A. A. F.

Figure Legend

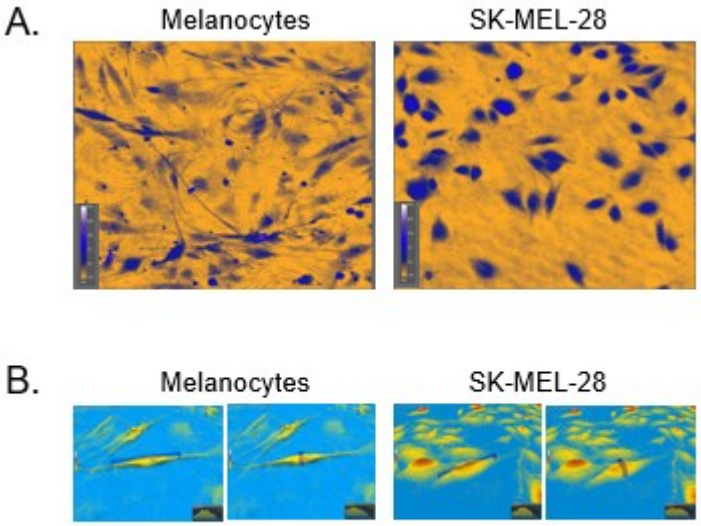


Figure 1. Holographic Microscopic Images (A) and Single Cell Thickness Measurements Across Length and Width (B) of Melanocytes and SK-MEL-28 cells.

This article is protected by copyright. All rights reserved.

Author Manuscript

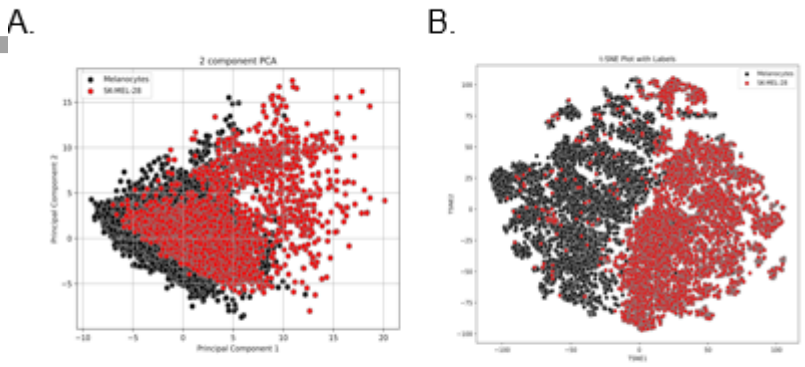


Figure 2. The Principal Component Analysis (PCA) plot and t-Distributed Stochastic Neighbor Embedding (t-SNE) Analysis of the Morphological Features of Normal Melanocytes and SK-MEL-28 Melanoma Cells. The PCA plot (A) reduces the high-dimensional morphological data into two principal components, providing a clear visual separation between the two cell types. The x and y axes denote the first two principal components. Normal melanocytes are represented in black, while melanoma cells are represented in red. The distinct clustering patterns indicate significant differences in their morphological characteristics. The t-SNE analysis (B) offers a two-dimensional projection of the high-dimensional morphological data, capturing the underlying structure and differences between the cell types. The x and y axes represent the two t-SNE dimensions. Similar to the PCA plot, normal melanocytes and melanoma cells form distinct clusters, emphasizing their morphological heterogeneity. Sample size was 10,114 for Melanocytes and 10,846 for SK-MEL-28. Multivariate analysis of variance (MANOVA) was performed to test for overall differences between the two cell types across all morphological features ($P < 0.001$). Post-hoc analyses using Bonferroni-corrected t-tests were conducted for each individual morphological feature ($P < 0.05$ for all features). Data are presented as individual data points in both PCA

This article is protected by copyright. All rights reserved.

Author Manuscript

and t-SNE plots. The clear separation of clusters in both PCA and t-SNE analyses suggests significant morphological differences between normal melanocytes and SK-MEL-28 melanoma cells.

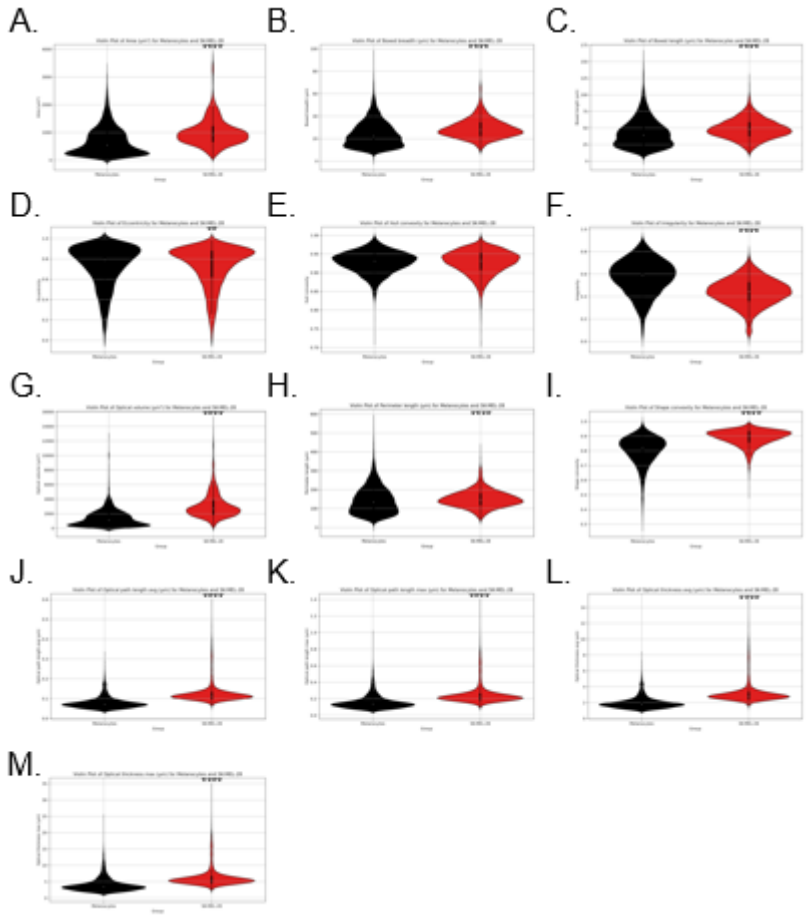


Figure 3. Violin Plots of Morphological Features for Melanocytes vs. SK-MEL-28.

Violin plots in the figure compare the morphological features of normal melanocytes and SK-MEL-28 melanoma cells. Melanocytes exhibit smaller and more concentrated distributions for cell area (A), boxed breadth (B), and boxed length (C) compared to SK-MEL-28 cells. Both cell types show similar eccentricity (D) and hull convexity (E) values. Melanocytes display higher irregularity (F), indicating more irregular shapes. SK-MEL-28 cells have larger optical volumes (G), longer perimeter lengths (H), and higher shape convexity (I). Additionally, SK-MEL-28 cells show greater average (J) and maximum (K) optical path lengths, as well as

This article is protected by copyright. All rights reserved.

Author Manuscript

higher average (L) and maximum (M) optical thickness. These plots highlight distinct morphological and optical differences between the two cell types. Sample size was 10,114 for Melanocytes and 10,846 for SK-MEL-28, whereas the probability value is shown in the figure, The meaning of the significance symbol (**** for $p < 0.0001$, ** for $p < 0.01$).

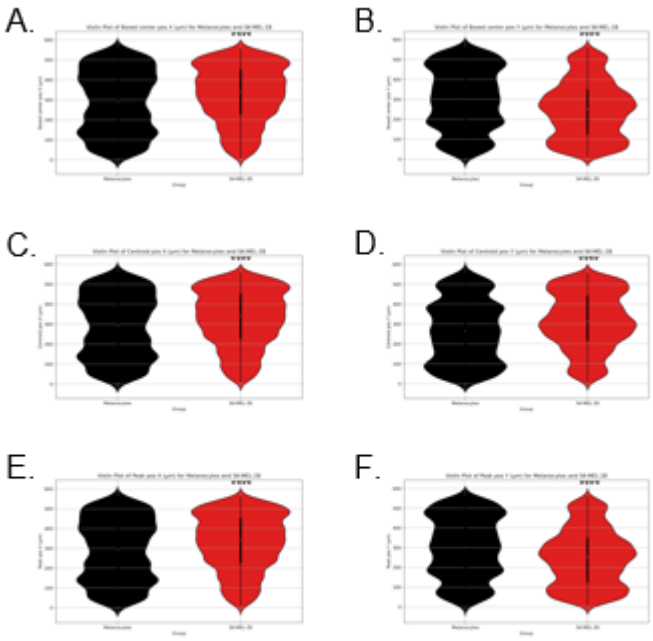


Figure 4. Violin Plots of Positional and Geometric Parameters for Melanocytes vs. SK-MEL-28. This figure presents violin plots comparing the positional and geometric parameters of normal melanocytes and SK-MEL-28 melanoma cells. Both cell types exhibit comparable distributions for boxed center position X (A) and Y (B), as well as centroid position X (C) and Y (D). The distributions of peak position X (E) and Y (F) show slight differences, with SK-MEL-28 cells displaying a broader range. These plots highlight the overall similarity in spatial positioning between the two cell types, with minor variations in peak positions. Sample size was 10,114 for Melanocytes and 10,846 for SK-MEL-28, probability value is shown in the

This article is protected by copyright. All rights reserved.

Author Manuscript

figure, the specific statistical test (Wilcoxon test) for each experiment, data presentation, and the meaning of the significance symbol (**** for p < 0.0001)

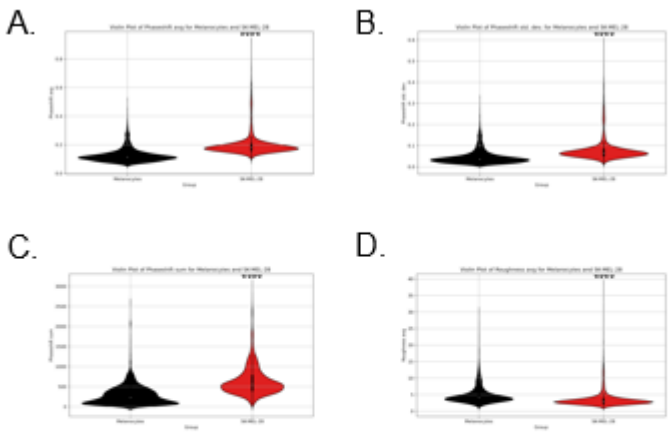


Figure 5. Violin Plots of Phase Shift and Roughness Parameters for Melanocytes vs. SK-MEL-28. This figure displays violin plots comparing the phase shift and roughness parameters of normal melanocytes and SK-MEL-28 melanoma cells. SK-MEL-28 cells exhibit consistently higher values for phase shift average (A), phase shift standard deviation (B), and phase shift sum (C) compared to melanocytes, indicating greater phase shift values and variability. Additionally, melanocytes show higher values for roughness average (D), suggesting greater surface roughness on average. These plots highlight significant differences in phase shift and surface roughness characteristics between the two cell types. Sample size was 10,114 for Melanocytes and 10,846 for SK-MEL-28, probability value is shown in the figure, the specific statistical test (Wilcoxon test) for each experiment, data presentation, and the meaning of the significance symbol (**** for p < 0.0001.

This article is protected by copyright. All rights reserved.

Author Manuscript

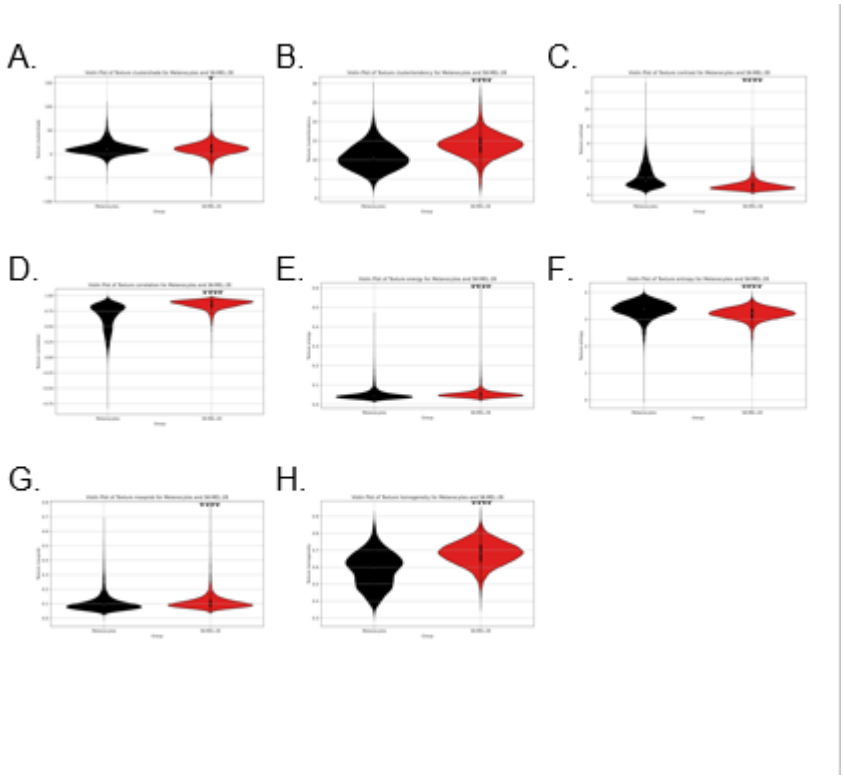


Figure 6. Violin Plots of Texture Parameters for Melanocytes vs. SK-MEL-28. Violin plots in this figure compare the texture parameters of normal melanocytes and SK-MEL-28 melanoma cells. Melanocytes exhibit higher values for texture clustershade (A), texture contrast (C), and texture entropy (F), indicating more variability and complexity in their texture. In contrast, SK-MEL-28 cells show higher values for texture clustertendency (B), texture correlation (D), texture energy (E), and texture homogeneity (H), suggesting more uniform and predictable textures. Both cell types have similar distributions for texture max probability (G). These plots highlight significant differences in the texture characteristics between melanocytes and SK-MEL-28 cells. Sample size was 10,114 for Melanocytes and 10,846 for SK-MEL-28, probability value is shown in the figure, the specific statistical test (Wilcoxon test) for each experiment, data presentation, and the meaning of the significance symbol (**** for $p < 0.0001$, * for $p < 0.1$).

This article is protected by copyright. All rights reserved.

Author Manuscript

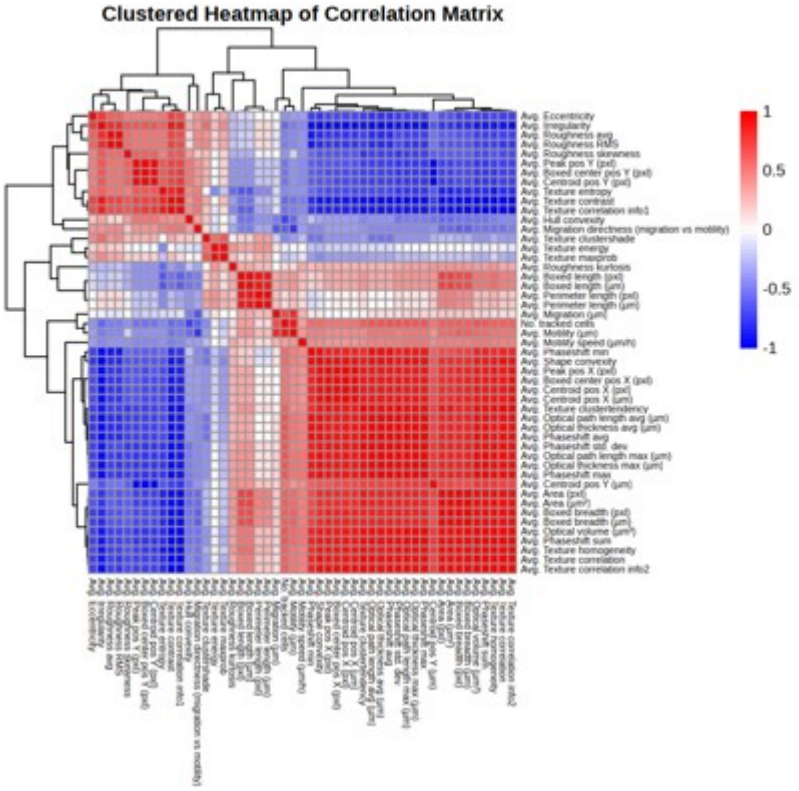


Figure 7. Clustered Heatmap of Correlation Matrix. A clustered heatmap of the correlation matrix for various morphological and optical parameters of cells was constructed. The heatmap illustrates the strength and direction of correlations between parameters, with the color gradient ranging from blue (indicating negative correlations) to red (indicating positive correlations). The hierarchical clustering on the rows and columns categorizes parameters with similar correlation patterns, revealing distinct clusters of highly correlated features. For example, parameters related to cell size and shape, such as optical thickness and optical volume, form a cluster with strong positive correlations. Conversely, parameters like irregularity and area show negative correlations with these size-related features. This visualization highlights the complex relationships between different cell characteristics, providing insights into the underlying data structure and guiding further analysis of cellular properties. The analysis was conducted on a sample size of 10,114 for Melanocytes and

This article is protected by copyright. All rights reserved.

Author Manuscript

10,846 for SK-MEL-28. The correlation matrix does not involve hypothesis testing, so there is no probability value associated with it.

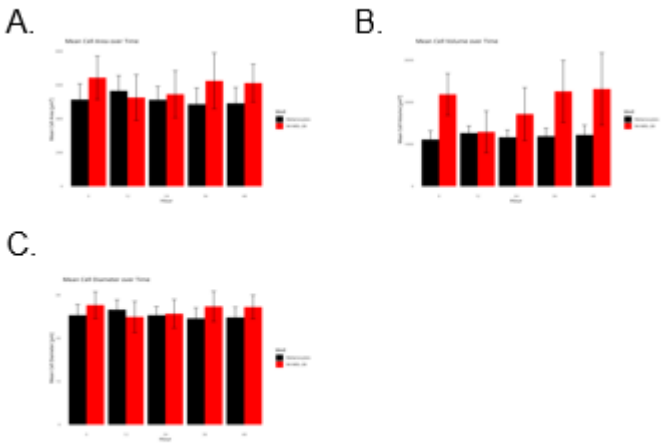


Figure 8. Mean Diameter, Area, and Volume of Melanocytes vs. SK-MEL-28 at Various Hours. This figure presents bar graphs comparing the mean cell area (A), mean cell volume (B), and mean cell diameter (C) of melanocytes and SK-MEL-28 cells at 0, 12, 24, 36, and 48 hours. Melanocytes (black bars) show a slight decrease in mean cell area and diameter over time, while SK-MEL-28 cells (red bars) exhibit higher and more variable values. In contrast, both cell types show an increase in mean cell volume, with SK-MEL-28 cells consistently having larger measurements. Error bars represent the standard deviation of the measurements, highlighting variability within the samples. These graphs underscore the greater size and growth of SK-MEL-28 cells compared to melanocytes over time.

This article is protected by copyright. All rights reserved.

Author Manuscript

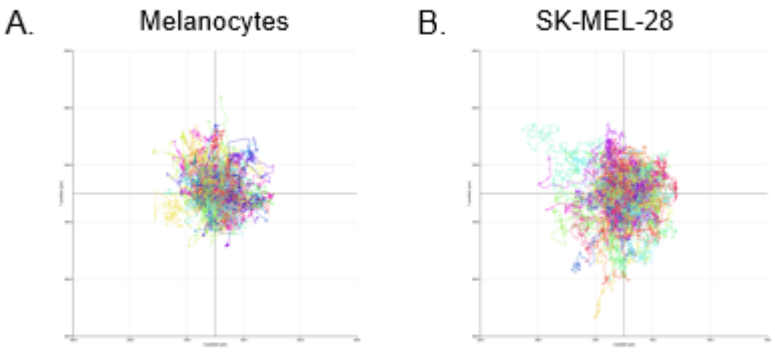


Figure 9. Cell Movement Plots for Melanocytes and SK-MEL-28. The cell movement plots compare melanocytes and SK-MEL-28 cells. Melanocytes (A): Movement is confined, with cells staying close to the origin. SK-MEL-28 (B): Movement is varied and extensive, with cells more likely to travel further and change direction frequently. These plots highlight the more dynamic migration behavior of SK-MEL-28 cells compared to melanocytes.

This article is protected by copyright. All rights reserved.

Author Manuscript

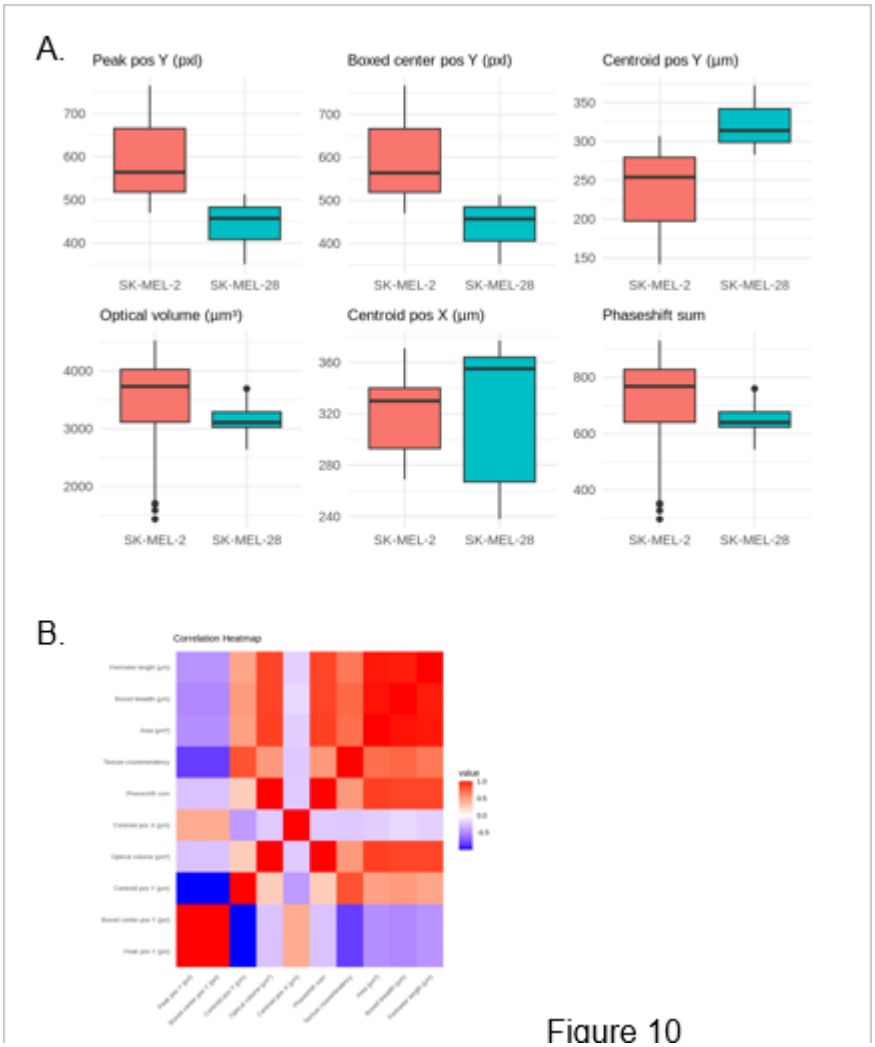


Figure 10. Heterogeneity in Morphological and Optical Characteristics of SK-MEL-2 and SK-MEL-28 Cell Lines. (A) Box plots of key features for SK-MEL-2 (red) and SK-MEL-28 (blue) cell lines. Features shown: Peak pos Y, Boxed center pos Y, Centroid pos Y, Optical volume, Centroid pos X, and Phaseshift sum. n = 10,000 cells/cell line. (B) Correlation heatmap of top 10 features. Color scale: blue (-1) to red (1). Statistical analysis: Mann-Whitney U test. **** $P < 0.0001$ for all comparisons in (A). Box plots show median (central line), 25th-75th percentiles (box), and 1.5x interquartile range (whiskers). Outliers as individual points. Heatmap shows Pearson correlation coefficients.

This article is protected by copyright. All rights reserved.

Author Manuscript

References

1. Bogenrieder, T. *Clinicopathological and molecular aspects of cutaneous Melanoma*. 2009.
2. Aladowicz, E., et al., *Molecular Networks in Melanoma Invasion and Metastasis*. Future Oncology, 2013. **9**(5): p. 713-726.
3. Leonardi, G.C., et al., *Cutaneous Melanoma: From Pathogenesis to Therapy (Review)*. International Journal of Oncology, 2018.
4. Oba, J. and S.E. Woodman, *The Genetic and Epigenetic Basis of Distinct Melanoma Types*. The Journal of Dermatology, 2021. **48**(7): p. 925-939.
5. Schadendorf, D., et al., *Melanoma*. The Lancet, 2018. **392**(10151): p. 971-984.
6. Satyamoorthy, K. and M. Herlyn, *Cellular and Molecular Biology of Human Melanoma*. Cancer Biology & Therapy, 2002. **1**(1): p. 14-17.
7. Olbryt, M., *Molecular background of skin melanoma development and progression: therapeutic implications*. Advances in Dermatology and Allergology/Postępy Dermatologii i Alergologii, 2019. **36**(2): p. 129-138.
8. Damsky, W.E., L.E. Rosenbaum, and M. Bosenberg, *Decoding Melanoma Metastasis*. Cancers, 2011. **3**(1): p. 126-163.
9. Jackett, L.A. and R.A. Scolyer, *A Review of Key Biological and Molecular Events Underpinning Transformation of Melanocytes to Primary and Metastatic Melanoma*. Cancers, 2019. **11**(12): p. 2041.
10. McLaughlin, A.J., et al., *Comparative Morphological Analysis of MCF10A and MCF7 Cells Using Holographic Time-lapse Microscopy*. AntiCancer Research, 2023. **43**: p. 3891 - 3896.
11. Palacios-Ortega, N., et al., *Measurement of morphology thickness and refractive index in a melanoma A375 cell line using digital holographic microscopy*. Applied Optics, 2021. **60**(4): p. 815-822.
12. Sober, A.J. and J.M. Burstein, *Computerized digital image analysis: an aid for melanoma diagnosis--preliminary investigations and brief review*. J Dermatol, 1994. **21**(11): p. 885-90.
13. Mackey, J.E. and D.A. Torigian, *Advanced Stages of Melanoma: Role of Structural Imaging*. PET Clin, 2011. **6**(1): p. 37-54.
14. Novita, G., et al., *Other Imaging Methods*, in *Breast Diseases*. 2019, Springer International Publishing AG: Switzerland. p. 65-71.

This article is protected by copyright. All rights reserved.

Author Manuscript

15. Desok, K. and Y. Young Il. *Cellular imaging-based biological analysis for cancer diagnostics and drug target development*. in *Proceedings. (ICASSP '05). IEEE International Conference on Acoustics, Speech, and Signal Processing, 2005.* 2005.

16. McLaughlin, A.J., et al., *Comparative Morphological Analysis of MCF10A and MCF7 Cells Using Holographic Time-lapse Microscopy.* Anticancer research, 2023. **43**(9): p. 3891-3896.

17. Pan, Z.J. *Principal Component Analysis Based Visualization and Human Melanoma Classification*. 2001.

18. Sharma, N., et al., *A Stochastic Neighbor Embedding Approach for Cancer Prediction.* 2021 International Conference on Emerging Smart Computing and Informatics (ESCI), 2021: p. 599-603.

19. Weitzman, J.B., *Mechanisms of melanoma metastasis.* Genome Biology, 2000. **1**(3): p. reports0067.

20. Croft, D.R. and M.F. Olson, *Regulating the conversion between rounded and elongated modes of cancer cell movement.* Cancer cell, 2008. **14 5**: p. 349-51.

21. Cochran, A.J., et al., *The shifting patterns of metastatic melanoma.* Clinics in laboratory medicine, 2000. **20 4**: p. 759-83, vii.

22. Ng, M.F., J.L. Simmons, and G.M. Boyle, *Heterogeneity in Melanoma.* Cancers, 2022. **14**.

23. Kabbarah, O. and L. Chin, *Revealing the genomic heterogeneity of melanoma.* Cancer cell, 2005. **8 6**: p. 439-41.

24. Sekulic, A., et al., *Malignant melanoma in the 21st century: the emerging molecular landscape.* Mayo Clinic proceedings, 2008. **83 7**: p. 825-46.

25. MÖLder, A., et al., *Non-invasive, label-free cell counting and quantitative analysis of adherent cells using digital holography.* Journal of microscopy (Oxford), 2008. **232**(2): p. 240-247.

26. Kemper, B., et al., *Label-free quantitative cell division monitoring of endothelial cells by digital holographic microscopy.* Journal of Biomedical Optics, 2010. **15**(3): p. 036009.

27. Dunn, A. and R. Richards-Kortum, *Three-dimensional computation of light scattering from cells.* IEEE Journal of Selected Topics in Quantum Electronics, 1996. **2**(4): p. 898-905.

28. Steike, D.R., et al., *Digital Holographic Microscopy for Label-Free Detection of Leukocyte Alternations Associated with Perioperative Inflammation after Cardiac Surgery.* Cells (Basel, Switzerland), 2022. **11**(4): p. 755.

29. Kastl, L., et al., *Quantitative phase imaging for cell culture quality control.* Cytometry A, 2017. **91**(5): p. 470-481.

This article is protected by copyright. All rights reserved.

Author Manuscript

30. Zhao, W., et al., *Studying the nucleated mammalian cell membrane by single molecule approaches*. PloS one, 2014. **9**(5): p. e91595-e91595.

31. Lee, K., et al., *Quantitative Phase Imaging Techniques for the Study of Cell Pathophysiology: From Principles to Applications*. Sensors, 2013. **13**(4): p. 4170-4191.

32. Marquet, P., C.D. Depeursinge, and P.J. Magistretti, *Review of quantitative phase-digital holographic microscopy: promising novel imaging technique to resolve neuronal network activity and identify cellular biomarkers of psychiatric disorders*. Neurophotonics, 2014. **1**.

33. Park, Y., C. Depeursinge, and G. Popescu, *Quantitative phase imaging in biomedicine*. Nature Photonics, 2018. **12**(10): p. 578-589.

34. Jo, Y., et al., *Quantitative Phase Imaging and Artificial Intelligence: A Review*. IEEE journal of selected topics in quantum electronics, 2019. **25**(1): p. 1-14.

35. Pinzaru, I., et al., *Rutin Exerts Cytotoxic and Senescence-Inducing Properties in Human Melanoma Cells*. Toxics, 2021. **9**(9): p. 226.

36. Cheng, F., et al., *Directed arginine deiminase evolution for efficient inhibition of arginine-auxotrophic melanomas*. Applied Microbiology and Biotechnology, 2015. **99**(3): p. 1237-1247.

37. Cichorek, M., et al., *Skin melanocytes: biology and development*. Postepy Dermatol Alergol, 2013. **30**(1): p. 30-41.

38. Lam, V.K., et al., *Quantitative scoring of epithelial and mesenchymal qualities of cancer cells using machine learning and quantitative phase imaging*. Journal of biomedical optics, 2020. **25**(2): p. 26002.

39. Rezaei, M., et al., *The expression of VE-cadherin in breast cancer cells modulates cell dynamics as a function of tumor differentiation and promotes tumor–endothelial cell interactions*. Histochemistry and cell biology, 2018. **149**(1): p. 15-30.

40. Nissim, N., et al., *Real-Time Stain-Free Classification of Cancer Cells and Blood Cells Using Interferometric Phase Microscopy and Machine Learning*. Cytometry. Part A, 2021. **99**(5): p. 511-523.

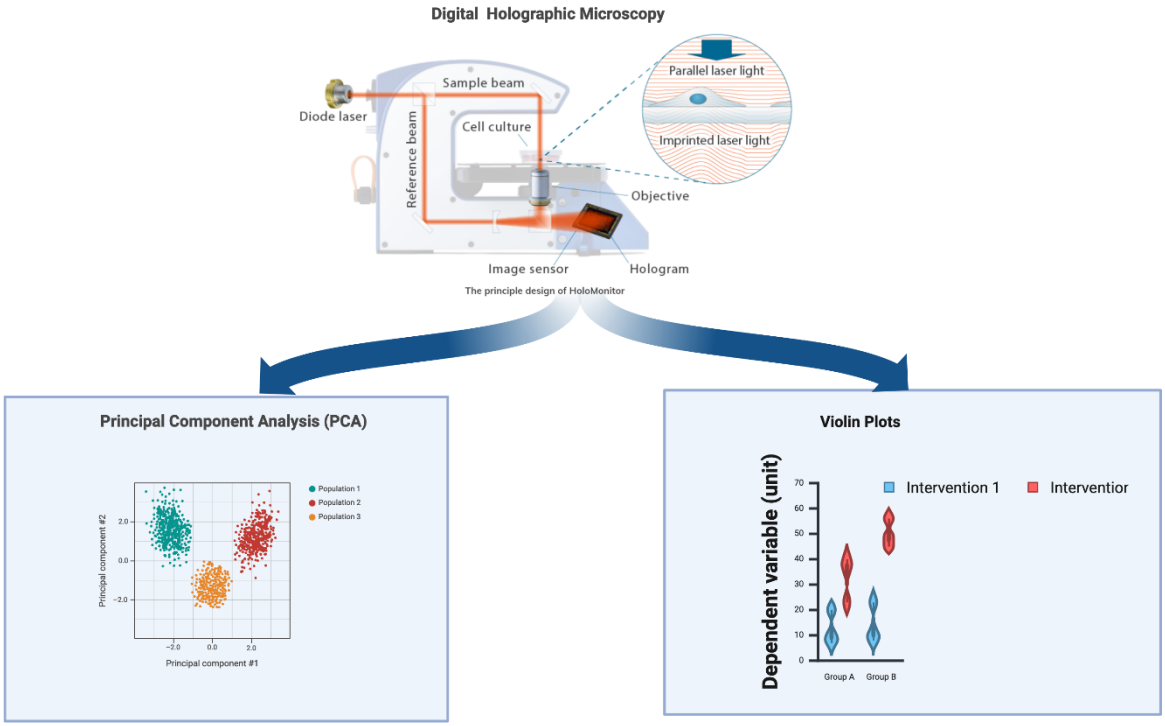
41. Pirone, D., et al., *Label-free liquid biopsy through the identification of tumor cells by machine learning-powered tomographic phase imaging flow cytometry*. Scientific reports, 2023. **13**(1): p. 6042-13.

This study compares the morphological and optical properties of melanocytes and SK-MEL-28 melanoma cells using digital holographic microscopy and quantitative phase imaging. It highlights significant differences in cell size, shape, surface roughness, and movement patterns. Techniques like PCA, t-SNE, and hierarchical clustering are used to identify distinguishing cellular characteristics.

This article is protected by copyright. All rights reserved.

Author Manuscript

Comparative Morphological and Optical Analysis of Melanocytes and SK-MEL-28 Cells



Created with BioRender.com

This article is protected by copyright. All rights reserved.